

High-dimensional brain-wide functional connectivity mapping in magnetoencephalography

Jose M. Sanchez-Bornot^{a,*}, Maria E. Lopez^{b,c}, Ricardo Bruña^{b,c,d}, Fernando Maestu^{b,c,d},
Vahab Yousofzadeh^e, Su Yang^f, David P. Finn^g, Stephen Todd^h, Paula L. McLeanⁱ,
Girijesh Prasad^a, KongFatt Wong-Lin^{a,*}

^a Intelligent Systems Research Centre, School of Computing, Engineering and Intelligent Systems, Ulster University, Magee campus, Derry, Londonderry, UK

^b Department of Experimental Psychology, Cognitive Processes and Speech Therapy Universidad Complutense de Madrid, Madrid, Spain

^c Networking Research Center on Bioengineering, Biomaterials and Nanomedicine, Madrid, Spain

^d Laboratory of Cognitive and Computational Neuroscience, Center for Biomedical Technology, Complutense University of Madrid and Technical University of Madrid, Madrid, Spain

^e Department of Neurology, Medical College of Wisconsin, Milwaukee, USA

^f Department of Computer Science and Software Engineering, Xi'an Jiaotong-Liverpool University, Jiangsu, China

^g Pharmacology and Therapeutics, School of Medicine, National University of Ireland Galway, Ireland

^h Altnagelvin Area Hospital, Western Health and Social Care Trust, Derry, Londonderry, UK

ⁱ Northern Ireland Centre for Stratified Medicine, Biomedical Sciences Research Institute, Ulster University, Northern Ireland, UK

ARTICLE INFO

Keywords:

Functional connectivity
Cluster permutation statistics
Nonparametric statistics
Multiple comparison correction
EEG and MEG biomarkers
Alzheimer's disease

ABSTRACT

Background: Brain functional connectivity (FC) analyses based on magneto/electroencephalography (M/EEG) signals have yet to exploit the intrinsic high-dimensional information. Typically, these analyses are constrained to regions of interest to avoid the curse of dimensionality, with the latter leading to conservative hypothesis testing.

New method: We removed such constraint by estimating high-dimensional source-based M/EEG-FC using cluster-permutation statistic (CPS) and demonstrated the feasibility of this approach by identifying resting-state changes in mild cognitive impairment (MCI), a prodromal stage of Alzheimer's disease. Particularly, we proposed a unified framework for CPS analysis together with a novel neighbourhood measure to estimate more compact and neurophysiological plausible neural communication. As clusters could more confidently reveal interregional communication, we proposed and tested a cluster-strength index to demonstrate other advantages of CPS analysis.

Results: We found clusters of increased communication or hypersynchronization in MCI compared to healthy controls in delta (1–4 Hz) and higher-theta (6–8 Hz) bands oscillations. These mainly consisted of interactions between occipitofrontal and occipitotemporal regions in the left hemisphere, which may be critically affected in the early stages of Alzheimer's disease.

Conclusions: Our approach could be important to create high-resolution FC maps from neuroimaging studies in general, allowing the multimodal analysis of neural communication across multiple spatial scales. Particularly, FC clusters more robustly represent the interregional communication by identifying dense bundles of connections that are less sensitive to inter-individual anatomical and functional variability. Overall, this approach could help to better understand neural information processing in healthy and disease conditions as needed for developing biomarker research.

1. Introduction

Functional connectivity (FC) analyses are continuously evolving, helping us to shape our understanding of network organization in

healthy and unhealthy brains (de Vos et al., 2018; Greicius et al., 2004, 2003; van den Heuvel and Hulshoff Pol, 2010). Typically, FC studies are conducted in resting-state since the associated spontaneous brain activity recruits multiple brain regions and networks, which can also be

* Corresponding authors.

E-mail addresses: jm.sanchez-bornot@ulster.ac.uk (J.M. Sanchez-Bornot), k.wong-lin@ulster.ac.uk (K. Wong-Lin).

<https://doi.org/10.1016/j.jneumeth.2020.108991>

Received 12 May 2020; Received in revised form 6 September 2020; Accepted 22 October 2020

Available online 9 November 2020

0165-0270/© 2020 The Authors.

Published by Elsevier B.V. This is an open access article under the CC BY-NC-ND license

(<http://creativecommons.org/licenses/by-nc-nd/4.0/>).

observed during active cognitive states (Buckner et al., 2013, 2009; Haak et al., 2018; Power et al., 2011; Raichle, 2015). Due to the consistency of resting-state FC results across multiple datasets, FC can also be used to study brain disorders (Buckner et al., 2009; de Vos et al., 2018; Greicius et al., 2004, 2003; Maestú et al., 2015). Furthermore, the use of resting-state functional magnetic resonance imaging (rs-fMRI) has attracted most attention given the excellent spatial resolution of fMRI to map brain function differences between conditions (Buckner et al., 2013; Haak et al., 2018). However, rs-fMRI analyses provide only an ultra-low frequency filtered and indirect representation of the underlying neural dynamics, as fMRI is based on the slow blood-oxygen-level dependent (BOLD) signal (Logothetis, 2008). In contrast, magneto-/electroencephalography (M/EEG) imaging resolves such limitations by directly reflecting transient neural dynamics and allowing to infer communication among brain regions (Hipp et al., 2012; O'Neill et al., 2018; Schoffelen and Gross, 2009; Tewarie et al., 2019).

In any case, either using fMRI (Buckner et al., 2013; Power et al., 2011; Raichle, 2015) or M/EEG (Dimitriadis et al., 2018; Hillebrand et al., 2012; Koelewijn et al., 2019; Yu et al., 2017) data, analyses are heavily reliant on the use of regions of interest (ROIs) for reducing dimensionality, with a trade-off between the advantages of faster computations and less-conservative statistical tests, versus the possible loss of information and biased results (Hillebrand et al., 2012; Zalesky et al., 2012a). Conversely, FC studies in the last decades have shown the feasibility of high-dimensional approaches to study network dynamics in greater detail (Hayasaka and Nichols, 2003; Hipp et al., 2012; Smith and Nichols, 2009; Zalesky et al., 2012a, 2012b, 2010; Zhang et al., 2018), e.g. using cluster-permutation statistic (CPS), with the critical advantage that significant network clusters ensure strong evidence of inter-regional connectivity (Zalesky et al., 2012a, 2012b, 2010; Zhang et al., 2018). Therefore, high-dimensional FC analysis could enhance the evaluation of FC differences between healthy and unhealthy brain conditions (Zalesky et al., 2012b; Zhang et al., 2018). However, the state-of-the-art of CPS is mostly limited to non-M/EEG data (Smith and Nichols, 2009; Zalesky et al., 2012a, 2012b, 2010; Zhang et al., 2018) or low-dimensional analysis (Mamashli et al., 2019; Maris and Oostenveld, 2007), and hence not fully exploiting the advantages of the CPS approach.

In this work, we extended the application of CPS to high-dimensional source-based M/EEG data, e.g. for source-based FC analysis after solving the M/EEG inverse problem. Specifically, we estimated source pairwise FC using our recently proposed connectivity measure to control for volume conduction effects (Sanchez-Bornot et al., 2018). By concurrently dealing with FC analysis in the intrinsic high-dimensional brain-source space while controlling for volume conduction, we demonstrated increased sensitivity of post-hoc statistical analyses. This approach was applied to a dataset of 30 healthy control (HC) and 30 mild cognitive impairment (MCI) participants, where MCI was diagnosed according to standard criteria (Albert et al., 2011). Statistical tests for the estimated FC differences between the HC and MCI groups, and for the covariation of these networks with respect to measured cognitive tests, were evaluated. We found significantly increased activation of occipitotemporal and occipitofrontal networks in MCI with respect to HC participants (hypersynchronization) in the left hemisphere, possibly associated with cognitive decline, and showed that significant FC clusters could be exploited for developing biomarker research in Alzheimer's disease (AD).

2. Materials and methods

2.1. Participants

Data were collected from a total of 60 participants at Hospital Universitario de San Carlos (Madrid, Spain), including eyes-closed resting-state magnetoencephalography (MEG) recordings and neuropsychological tests scores: mini-mental-state-examination (MMSE) Spanish

version (Lobo et al., 1980), and delayed/immediate recall memory (DRM/IRM) scores from Wechsler Memory Scale-III (Wechsler, 1997). Inclusion criteria: recruitment age of 65–85 years, right-handed as verified using Edinburgh Handedness Inventory (Oldfield, 1971), native Spanish speakers, a modified Hachinski score ≤ 4 (Rosen et al., 1980), a Geriatric Depression Scale short-form score ≤ 5 (Reisberg et al., 1982), and no indication of comorbidities or brain trauma according to MRI inspection (López et al., 2014). MCI participants showed signs of hippocampal atrophy as quantified using their anatomical MRI, and therefore it was considered that their cognitive impairment was related to AD pathology with an intermediate likelihood (Albert et al., 2011). HC group: N = 30, 16 females, ages 66–80 years. MCI group: N = 30, 15 females, ages range 65–78 years (see Table 1 for further details). Informed consent was obtained from all the participants in conformity with the Declaration of Helsinki (1991), and the study was approved by the local ethical review board.

2.2. MEG data recording

The MEG signals were acquired using an Elekta-Neuromag system with 306 channels (102 magnetometers and 204 planar gradiometers) with a sampling frequency of 1 kHz and online anti-alias filter with 0.1–330 Hz bandwidth. Concurrently, head movements were tracked using a continuous head-position indicator (cHPI) with four coils attached to the scalp. The position for these coils, fiducial points (nasion, and left/right preauricular), and head-shape model were digitised using a three-dimensional Fastrak Polhemus system (Polhemus, Inc, USA). Additionally, bipolar electro-oculogram sensors were attached above and below the left eye to measure ocular movements, and an electrical ground electrode was attached to the earlobe. With these conditions, three-minute MEG resting-state recordings were acquired for all participants. During the acquisition, they were instructed to remain calm and control their movement as long as possible, while an expert supervised the session to ensure that participants remained in an awake state. Offline, the recorded MEG signals were processed using the temporal extension of the signal-space separation technique (Maxfilter version 2.2, Elekta; correlation threshold = 0.9, time window = 10 s) to reduce the contribution of external magnetic field and correct for the head movements using the cHPI data. However, we found non-significant differences of head movement between both groups ($p \approx 0.68$), with an average Euclidean distance (reference: initial head position) of 3.3 mm (± 2.5) and 3.7 mm (± 2.9) for the HC and MCI groups, respectively.

2.3. Pipeline for data preparation

Data preparation for post-hoc analyses was conducted using a MATLAB custom code based on SPM12 and Fieldtrip tools. The first step

Table 1

Participants' demographics. The p-values were obtained by two-independent samples *t*-test (*) or chi-square test (+). HC = Healthy Control; MCI = Mild Cognitive Impairment; M = Male; F = Female; MMSE = Mini-Mental State Examination; IRM: Immediate Recall Memory; DRM: Delayed Recall Memory; RH_ICV and LH_ICV: right and left hippocampal volume normalised with intracranial volume, respectively. Highest education completed, using five levels: 1. Illiterate, 2. Primary studies, 3. Elemental studies, 4. High school studies, and 5. University studies.

	HC group (N = 30)	MCI group (N = 30)	p-values
Age (years)	72.1 \pm 4.1	72.2 \pm 4.0	0.874*
Gender (M/F)	14/16	15/15	0.796+
Educational level	3.6 \pm 1.1	3.4 \pm 1.3	0.707*
MMSE	29.2 \pm 0.8	26.9 \pm 1.9	<1e-6*
IRM	38.7 \pm 8.0	18.9 \pm 9.0	<1e-8*
DRM	24.6 \pm 6.6	7.2 \pm 8.0	0.089*
RH_ICV	0.00250 \pm 0.00030	0.00207 \pm 0.00047	0.0002*
LH_ICV	0.00251 \pm 0.00035	0.00207 \pm 0.00046	0.0002*

is to obtain meshes for the cortical surface of each individual. This was implemented by using the SPM12's "normal" size template mesh, with 8196 vertices fairly distributed over the cortical surface (4098 vertices per hemisphere, excluding cerebellum, ~ 5 mm source-to-source separation). This SPM12's template mesh is available within the software files and was initially obtained from an exemplar individual using BrainVISA/Anatomist (Litvak et al., 2011; Mattout et al., 2007). Moreover, it was demonstrated with data from nine individuals that the fitting of the SPM12's canonical mesh to a new individual brain, via nonlinear warping, resulted in superior results in comparison to using a fixed template brain, and comparable results to those obtained from cortical meshes directly extracted from the individual brain (Henson et al., 2009). Therefore, in our study we followed this procedure for obtaining individual meshes by warping the SPM12's "normal" size mesh into the individual brains, which is an automatic process as implemented in SPM12. Not least important, in the second step, the individually warped canonical mesh is co-registered with the sensors space using the location for the MEG sensors and Philemus' digitised headshape points. Although this is also an automatic step as implemented in SPM12, we preferred in our study to use a modified interface based on the automatic SPM12's co-registration routine to improve the accuracy (see Supp. Fig. 1). As outcome from the implementation of these two steps, we obtained the location for the brain sources in our study, as they corresponded to the 8196 vertices in the individual meshes, and the MEG lead-fields for these sources using the single-shell Boundary Element Method, as it can be calculated in SPM12 directly after the co-registration step, correspondingly for a perpendicular dipole orientation constraint (Henson et al., 2010, 2009).

Similarly, using the SPM12 toolbox within a MATLAB custom script, signals were pre-processed using a Butterworth's bandpass filter of 0.5–48 Hz bandwidth, downsampled to 200 Hz and epoched into 2-second segments (90 trials) using a Hann window. Although highly recommended in other pipelines, notice that we do not reject artifact signals in our pipeline as we use a FC measure which is robust to volume conduction, as discussed below. Next, source reconstruction analysis was conducted using the SPM12's Bayesian minimum norm implementation (Mattout et al., 2006), separately for each segment. Finally, the discrete Fourier transform (MATLAB fft function) was applied to each estimated and epoched source activity, and its derived complex numbers were halved to "single" precision and saved to hard disk for post-hoc FC analyses. In summary, this resulted in a 3D matrix of dimensions 96 frequency bins (frequency resolution of 0.5 from 0.5 to 48 Hz), 8196 sources and 90 segments, for each subject.

2.4. Pipeline for FC analysis

Specifically, in this study the envelope of the imaginary coherence (EIC) was estimated as the FC measure between two signals $x_i(t)$ and $x_j(t)$, for each frequency f (Sanchez-Bornot et al., 2018):

$$EIC_{ij}(f) = \left| \frac{\Im \left(\frac{1}{N} \sum_{n=1}^N \Im \{ X_{in}(f) X_{jn}^*(f) \} \right)}{\sqrt{\frac{1}{N} \sum_{n=1}^N \left| \Im \{ X_{in}(f) X_{jn}^*(f) \} \right|^2}} \right|^2$$

where $X_{in}(f)$ is the Fourier transform complex number output for signal $x_{in}(t)$, estimated separately for each epoch $n = 1, \dots, 90$, the operator $\Im(\cdot)$ extracts the imaginary part of the argument's complex number, and $|\cdot|$ stands for the absolute value. The above EIC formula produces a normalised measure of FC strength with values between 0 and 1, similar as with the coherence measure (Sanchez-Bornot et al., 2018). In this equation, considering the outcome of the imaginary operation as $z(f) =$

$\Im(\cdot)$, the Hilbert's transform $h(f) = \mathcal{H}(\cdot)$ allows us to obtain the EIC measure by estimating the analytical signal of the imaginary part, i.e. $h(f) = z(f) + i\tilde{z}(f)$, where $\tilde{z}(f)$ is obtained as (Zygmund, 2002):

$$\tilde{z}(f) = -\frac{1}{\pi} \lim_{\epsilon \rightarrow 0} \int_{\epsilon}^{+\infty} \frac{z(f+\omega) - z(f-\omega)}{\omega} d\omega$$

Due to limited RAM memory for conducting the statistical analyses, it is troublesome to directly compute the whole connectivity matrix of $8196 \times 8195/2$ interactions. Therefore, we partitioned the FC matrix into a 16×16 sub-block matrices for a total of $C_2^{17} = 136$ blocks (15 blocks times 500 sources + 1 block times 696 sources = 8196). We only kept the block subindices for the strictly upper triangular matrix due to the symmetry of the FC measure (Supp. Fig. 2). After the block-wise FC estimation, the EIC values were averaged for the interested frequency bands. These bands were chosen by partitioning the classical M/EEG band into 8 subbands to allow a slightly higher level of detail (delta δ : 0.5–4 Hz; lower-theta θ_1 : 4–6 Hz; upper-theta θ_2 : 6–8 Hz; lower-alpha α_1 : 8–10.5 Hz; upper-alpha α_2 : 10.5–13 Hz; lower-beta β_1 : 13–20 Hz; upper-beta β_2 : 20–30 Hz; gamma γ : 30–48 Hz). Thus, resulting in a total of $8 \times 8196 \times 8195/2$ FC measures, or about 0.27 billion features. Finally, these features were saved to hard disk, separately for each participant, frequency band and block, for post-hoc statistical analyses.

2.5. Nonparametric statistical analyses

Our study involves a feature matrix of 60 rows (30 HC and 30 MCI participants measurements with HC data stacked first) and about 0.27 billion columns, where the features corresponded to the estimation of $C_2^{8196} = 33,583,110$ pairwise FC for each of the mentioned frequency bands, together with the score vectors for the cognitive tests that were tested on each participant (one or two missing data in each test; same row order between the score vectors and the feature matrix). These measurements are used for: (i) the Wilcoxon rank-sum analysis of the differences between HC and MCI groups, and (ii) the Spearman rank-correlation analyses between each cognitive test (vector) and feature (matrix columns).

In our case, the estimated FC and cognitive scores are nonnegative and hardly follow the normality assumption. Therefore, we adopted a whole non-parametric framework to implement our cluster-permutation approach as discussed below. Non-parametric tests not only can produce more accurate results than comparable traditional techniques (Hollander et al., 2013), but also are often used to exploit relevant data structure, such as when using the permutation technique to exploit spatial smoothness (Hayasaka and Nichols, 2003; Zalesky et al., 2012a, 2012b, 2010).

The permutation technique is adopted here to create surrogate data under the null-hypothesis of no group differences between the observations in the feature matrix or no-monotonic relationship between each feature and cognitive scores, as discussed below with more technical

details for the Wilcoxon and Spearman analyses, respectively. Simply stated, each surrogate data is created by randomly reshuffling the row-order of the feature matrix in the Wilcoxon analysis, or the order of vector scores in the Spearman analysis ($N = 1000$ Monte Carlo simulations in our study). In the Wilcoxon analysis, notice that all the elements in each row of the matrix must be jointly reshuffled in order to create surrogate data while preserving the data structure. Particularly, the row

reshuffling corresponds to randomly assigning each subject to either the HC or MCI group, accordingly to the hypothesis of no group differences (Hayasaka and Nichols, 2003). This data-driven approach is critical for testing the significance of FC clusters as discussed below.

The implementation of our statistical framework is a computational challenge because the Wilcoxon and Spearman analyses produce an array of 0.27 billion p-values for the original and each of the 1000 surrogate data. Therefore, we adopted the suprathreshold technique (Hayasaka and Nichols, 2003; Zalesky et al., 2012a, 2012b, 2010) to select only those features with corresponding p-values lower or equal than a threshold of $p_1 = 10^{-7}$, $p_2 = 10^{-6}$, or $p_3 = 10^{-5}$, for the lower tail distributions, or greater or equal than $1 - p_1$, $1 - p_2$, or $1 - p_3$, for the upper tail distributions, for respectively measuring negative and positive effects. Subsequently, the suprathreshold connection indices were extracted from the selected features, for each separate frequency band, with FC indices in the range $\{1, \dots, C_2^{8196}\}$ and, finally, these indices were saved to hard disk for the posterior CPS analysis.

Note that for 0.27 billion features, using the mentioned thresholding strategy, the expected number of spuriously selected features is about 27, 270, or 2700, correspondingly to the above-defined suprathresholds. However, the probability for these “false positive” connections to agglomerate in clusters by chance or, similarly, the probability to observe a cluster with high cardinality by chance, is expected to be much lower than for the discovered FC corresponding to the actual networks, which is the principal motivation beyond using this approach. Moreover, we expect to obtain significant clusters of different sizes depending on the specific chosen suprathreshold value. Specifically, we could obtain narrower extended clusters for more conservative p-values ($p_1 = 10^{-7}$), while wider clusters could be obtained for higher p-values ($p_3 = 10^{-5}$).

Recall that the above analyses were conducted for the upper triangular part of the 8196×8196 FC matrix. After partitioning the upper-triangular matrix into 136 sub-blocks (Supp. Fig. 2), the statistical analyses were conducted block-wise due to RAM limitations. Afterwards, we loaded the suprathreshold FC indices for each block, separately for each frequency band, and assembled the indices for all the blocks before running the cluster parcellation procedure, which will be discussed in the next section. As a summary, this first stage of the implementation of our approach can be presented as follows:

- 1 FC data, or features, were loaded for all the participants, separately for each block and frequency band.
- 2 Wilcoxon and Spearman analyses, which were based on each of the 0.27 billion features and cognitive scores, were conducted for the original and each of the 1000 surrogate data, thus producing the corresponding p-values for each feature.
- 3 The suprathreshold values $p_1 = 10^{-7}$, $p_2 = 10^{-6}$, and $p_3 = 10^{-5}$, were used separately for selecting the corresponding suprathreshold features for negative and positive effects.
- 4 Only the FC indices corresponding to the suprathreshold features, were saved to hard disk for the posterior cluster parcellation.

2.6. Cluster-permutation statistical analysis

Our approach follows the same path for extending the application of cluster-permutation techniques to neuroimaging data by proposing a new neighbourhood measure, as done in previous studies (Zalesky et al., 2012a, 2010; Zhang et al., 2018). For example, the network-based statistic (NBS) proposes the creation of clusters by considering a neighbourhood relationship where two connections are regarded as neighbours if they share a node, thus expanding graph components (see Fig. 1 in Zalesky et al., 2010). Similarly, the spatial pairwise clustering (SPC) statistic checks whether there is a simultaneous match or neighbourhood relationship between the connections endpoints (see Fig. 3 in Zalesky et al., 2012a). Here, we instead introduce a novel

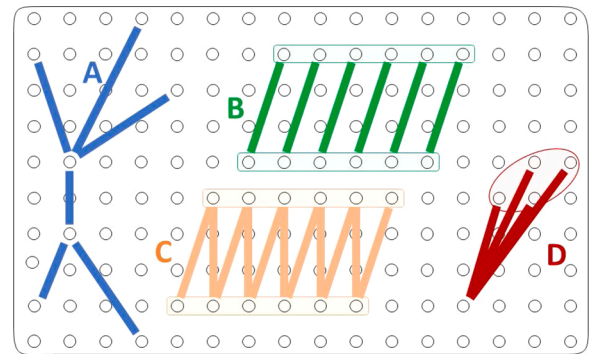


Fig. 1. Essential differences among the clustering criteria for network-based statistics (NBS), spatial pairwise clustering (SPC) and our novel criterion. Each line represents a connection derived from FC analysis, while the circles represent the nodes (brain sources). Clusters A-D are represented separately, enclosed within different shadowed regions and drawn using different colours. These clusters can be discovered using different neighbourhood measures as follows. For the NBS statistic, two connections are neighbours if they share a node, then any connected component is a cluster, i.e. A, C and D. SPC detects as neighbours those connections which endpoints are spatial neighbours, thus it finds that B, C and D are clusters using the von Neumann neighbourhood. Our SPC proposed modification introduces a more restrictive criterion: two connections are neighbours if and only if they share one endpoint while the other endpoints are spatial neighbours; thus, it considers that only C and D are clusters.

neighbourhood measure where two connections are considered neighbours if and only if they share one endpoint while the other endpoints are spatial neighbours (see Fig. 1). Furthermore, we note that the SPC relies on a more restrictive criterion of neighbourhood than NBS, whereas our criterion is more restrictive than SPC's. As a result, our method's detected clusters can always be identified by SPC, and SPC's clusters can always be identified by NBS, but not the other way around (Fig. 1).

In the following sections, therefore, we shall consider a unified framework to implement CPS analysis with the use of a neighbourhood measure. Using this framework, the second and last stage of our statistical analysis is stated as follows:

- 1 For each frequency band and for each suprathreshold value $p_1 = 10^{-7}$, $p_2 = 10^{-6}$, or $p_3 = 10^{-5}$, suprathreshold FC indices are loaded for all the blocks and assembled together in the range $\{1, \dots, C_2^{8196}\}$, separately for the selected suprathreshold features for negative and positive effects.
- 2 Using the assembled indices, clusters are estimated based on a neighbourhood measure and using the breadth-first search algorithm (see Supp. Table 1 for a practical implementation), separately for the original and 1000 surrogate data.
- 3 The number of connections, or cluster size, is computed for each cluster of the original and surrogate data.
- 4 The maximum-cluster-size statistic is calculated as the maximum size among all the clusters that were estimated for each surrogate data, which includes the clusters estimated for all the frequency bands and negative/positive effects, separately for each suprathreshold p-value. Thus, rendering a distribution of 1000 samples of this statistic in our analysis for each suprathreshold p-value.
- 5 The 95th percentile of the maximum-cluster-size distribution is then selected as the critical value, depending only on the suprathreshold p-value.
- 6 Finally, separately for each suprathreshold p-value, the significant FC clusters in the original data are those clusters with size greater or equal than the corresponding critical value.

2.7. Measure of cortico-cortical FC neighbourhood

Our novel neighbourhood measure is presented here in detail for our case where connections are between brain sources located in the cortical surface, rather than in a two-dimensional grid as introduced above in Fig. 1. Set $(X_{I_1(k)}, X_{I_2(k)})$, $I_1(k) < I_2(k)$, and $(X_{I_1(l)}, X_{I_2(l)})$, $I_1(l) < I_2(l)$, as a pair of connections defined for the strictly upper-part of a triangular matrix that is representing a symmetric FC measure, where the unique connections are arranged using an array of FC indices $1 \leq k, l \leq C_2^{8196}$, $k \neq l$, and $I(k) = (I_1(k), I_2(k)) : \{1, \dots, C_2^{8196}\} \mapsto \{1, \dots, 8195\} \times \{2, \dots, 8196\}$ is a functional mapping of the connection index to its corresponding vertices indices. Thus, $(X_{I_1(k)}, X_{I_2(k)}) : \{1, \dots, C_2^{8196}\} \mapsto \mathcal{S}^3 \times \mathcal{S}^3$.

Based on this definition, our FC neighbourhood measure can be calculated as follows:

- 1 Given two connections represented by its indices k and l , $1 \leq k, l \leq C_2^{8196}$, $k \neq l$, check whether $I_m(k)$ is equal to $I_n(l)$ for some $m, n \in \{1, 2\}$.
- 2 If true, then these connections have a vertex in common. Set $J(k)$ and $J(l)$ as the complementary vertices in the connections, i.e. $J(k) = I_{3-m}(k)$ and $J(l) = I_{3-n}(l)$. Notice that $J(k) \neq J(l)$ by definition.
- 3 Finally, these connections are neighbours if the vertices $X_{J(k)}$ and $X_{J(l)}$ are neighbours in the cortical surface (see Supp. Fig. 3).

2.8. Efficient computation of statistics within the CPS approach

Another improvement that we are introducing with respect to state-of-the-art CPS techniques is the application of computational tricks for dealing efficiently with the calculations within the permutation procedure. For example, naively, when running the Wilcoxon rank-sum statistic, the measures ranks are computed for the array of $M = 60$ participant measurements within each permutation. However, that will be inefficient as it involves an order of $O(M \log(M)N)$ operations, where N is the number of Monte-Carlo permutations. Because the measurements are fixed along permutations, we just need to sort the measurements at the initial step and then the rank-sum statistic can be updated linearly after each permutation, with a lower cost of $O(MN)$ operations (see Supp. Table 2 for a MATLAB code with the implementation of this idea).

Similarly, the Spearman rank-correlation analysis is based on the measurements ranks, thereby the rank estimation could be optimised as previously. Furthermore, in the correlation formula for the rank-correlation analysis between FC and cognitive scores we don't need to perform all the calculations for each permutation step. Clearly, as this formula can be expressed as

$$C(x, y) = \frac{\sum_{i=1}^M (x_i - \bar{x})(y_i - \bar{y})}{\sqrt{\sum_{i=1}^M (x_i - \bar{x})^2} \sqrt{\sum_{i=1}^M (y_i - \bar{y})^2}} = \frac{\sum_{i=1}^M x_i y_i - M \bar{x} \bar{y}}{\sqrt{\sum_{i=1}^M (x_i^2 + y_i^2) - M(\bar{x}^2 + \bar{y}^2)}}$$

then the numerator term $M \bar{x} \bar{y}$, and the whole denominator can be computed once. The only term that needs to be recomputed for each permutation is $\sum_{i=1}^M x_i y_i$. In summary, the intertwining of statistics and permutation calculations is feasible and has a significant impact on the speed of the whole procedure

Finally, another apparently less significant but very important trick is to use the suprathreshold statistical values, instead of the corresponding suprathreshold p-values. Therefore, within our implementation of the cluster-permutation procedure, we avoided estimating p-values for the involved statistical analysis. Interestingly, the most important aspect of this trick is that usually p-values for the Wilcoxon

and Spearman analyses are obtained using approximations because of the computational cost of using an accurate p-value computation. In our work, we created a lookup table for the Wilcoxon rank-sum statistic, which allowed to obtain the needed suprathreshold statistical values. For example, for our rank-sum statistic involving 30 HC vs. 30 MCI, we used the table values of 579, 603 and 629 for the lower tail of the statistical distribution, and 1251, 1227 and 1201 for the upper tail, correspondingly to the suprathreshold p-values of $p_1 = 10^{-7}$, $p_2 = 10^{-6}$, or $p_3 = 10^{-5}$, respectively (see Supp. Fig. 4). For the Spearman rank-correlation analysis, due to the high number of participants ($M = 60$), it is difficult to obtain an accurate p-values lookup table as the exact method involves an order of factorial of M operations. Therefore, for simplicity, for the Spearman analysis we used suprathreshold correlation values that were estimated using the standard p-value approximation for the Pearson's correlation coefficient that is based on the Student's t-distribution, i.e. $t = \hat{r} \sqrt{n-2} / \sqrt{1-\hat{r}^2}$, where \hat{r} is the estimated correlation coefficient, and the p-value is estimated as $2P(T > t)$, where T follows a t-distribution with $n-2$ degrees of freedom.

Summarising our approach, Fig. 2 shows a roadmap for the implementation of our analyses. Firstly, the MEG data was obtained from a dataset including 30 HC and 30 MCI participants (Fig. 2A, top). Secondly, a Bayesian minimum norm method (Mattout et al., 2006) was applied to estimate source time series in 8196 locations of the individual cortical surface, separately for each participant (Fig. 2A, bottom; Fig. 2B, top). Thirdly, after the spectral analysis of the source activity using Fourier transform, FC maps were derived using EIC (Sanchez-Bornot et al., 2018). The FC maps were computed directly for all the source pairs, an upper-triangular matrix of $8196 \times 8195/2$ elements and averaged across the selected frequency bands (Fig. 2B, bottom). These calculations were performed separately for each participant and, finally, the outcome consisting of a matrix of 60 rows and about 0.27 billion columns was submitted for post-hoc statistical analyses (Fig. 2C).

2.9. Data availability

The data of the present study would be available through an institutional repository and under a previous request to the authors.

2.10. Code availability

The MATLAB code is available at the following GitHub repository: <https://github.com/JMSBornot/High-Dimensional-Source-MEG-FC>.

3. Results

3.1. High-dimensional FC analysis can detect brain-wide communication

We will focus on source MEG-FC analysis to demonstrate our approach with very high dimensional data. Particularly, the FC maps were obtained using EIC, which allows to estimate both short-range and long-range connections while controlling for volume conduction artefacts (Sanchez-Bornot et al., 2018). Our analyses also include neuropsychological tests scores for the assessment of participants' cognitive abilities (MMSE, IRM and DRM). These measures were used to study the FC differences between HC and MCI participants using the nonparametric Wilcoxon rank-sum test, and the monotonic relationship between the FC strength and neuropsychological tests scores using the nonparametric Spearman rank-correlation test.

With about 0.27 billion features, the effect size of these statistical analyses must be noticeable to be successfully measured while controlling for multiple comparisons (Zalesky et al., 2010). For this purpose, we first used false discovery rate (FDR) (Genovese et al., 2002) and found significant relations in the rank-correlation analyses only between FC and DRM/IRM scores. In the analysis with DRM, we used FDR parameter $q = 0.05$ and found the significant p-values lower than 10^{-7} ($p < 10^{-7}$)

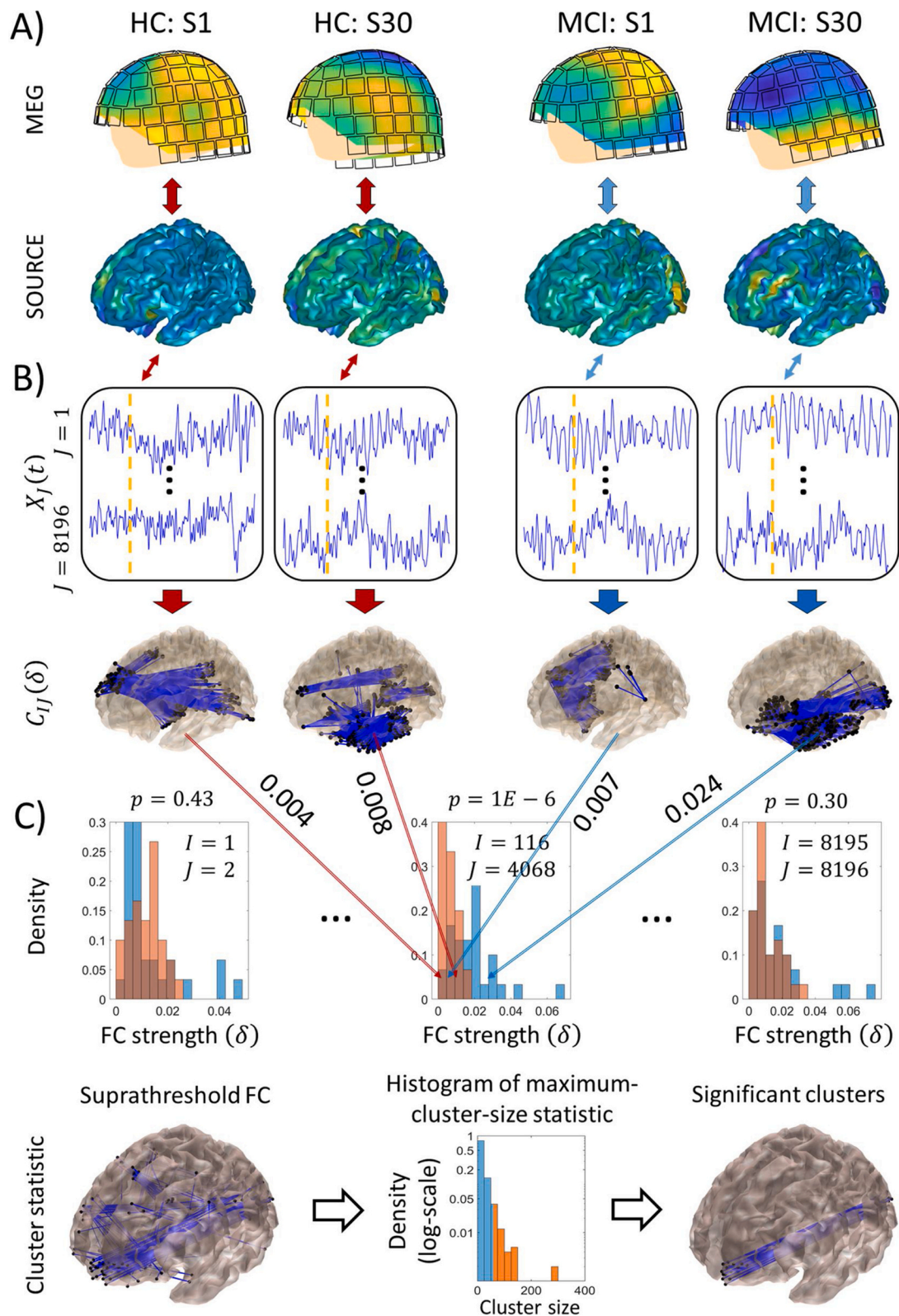


Fig. 2. Flowchart from MEG data to functional connectivity (FC) and statistical analysis. (A) Top: MEG signals are collected from 102 magnetometers and 204 planar gradiometers, for a dataset of 30 HC (HC: S1-30, left) and 30 MCI (MCI: S1-30, right) participants. Bottom: After pre-processing, source activity is estimated using Bayesian minimum norm for source reconstruction. (B) Time-series of estimated source activity segmented into nonoverlapping epochs (top) to produce FC maps for 8196 sources, where only the suprathreshold connections for communication at δ band are shown for clarity (bottom). (C) Top: Wilcoxon rank-sum analysis of FC strength differences between HC (red colour) and MCI (blue) participants, as revealed by the colour-bar histograms and statistic p-values for the selected connections with subindices I, J . Bottom: The connections with suprathreshold p-values are submitted to cluster-permutation statistical analysis for detecting significant clusters while controlling for multiple comparisons.

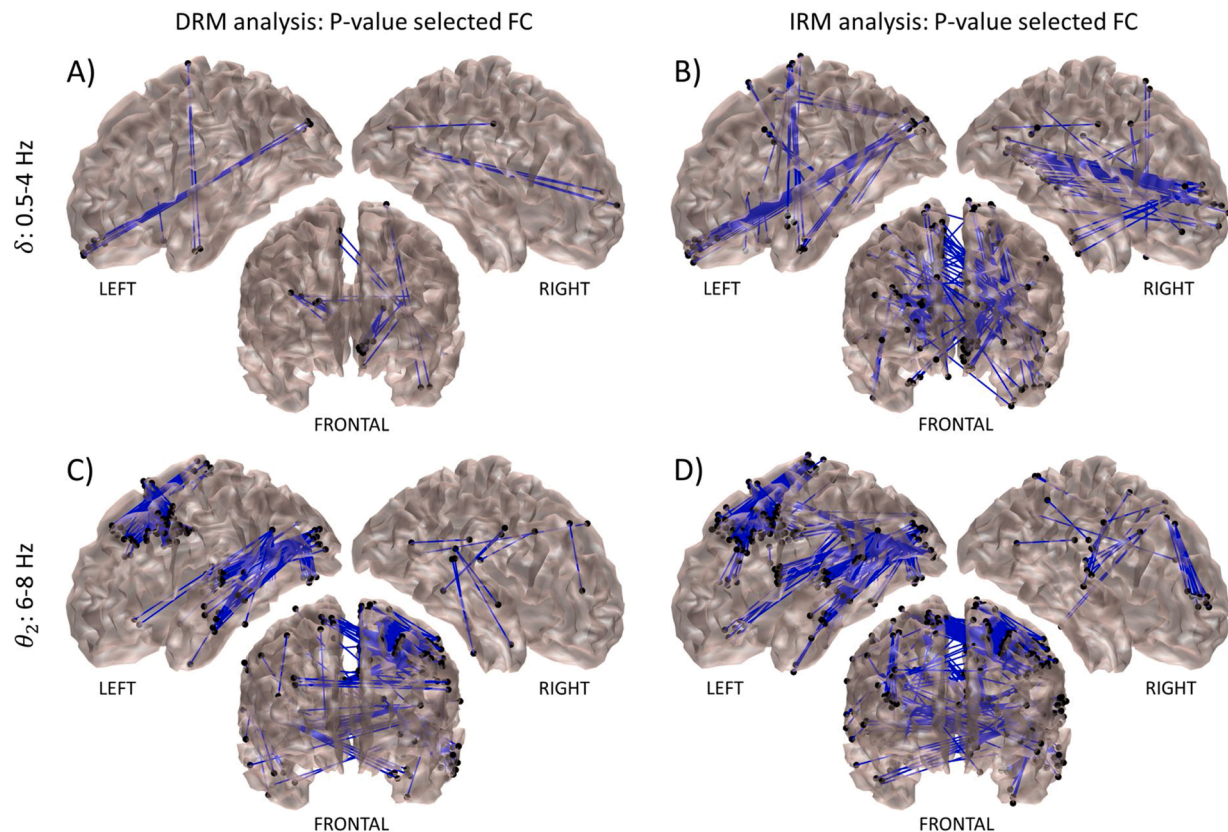


Fig. 3. Cortical maps of FC significantly correlated with cognitive (DRM or IRM) scores. Each FC map is topographically presented in three views: left/right lateral views of the cortical hemispheres and frontal view. The left/right view only shows connections between regions in the same hemisphere, whereas the frontal view shows all the significant FC. (A–B) Significant FC in δ band (see Table 2). (C–D) Significant FC in θ_2 band. Significant correlation of FC strength with cognitive scores was tested using FDR for both DRM and IRM tests, with FDR parameter $q = 0.05$ for DRM and $q = 0.2$ for IRM test. A higher value of q was needed for IRM test as it was less sensitive than DRM.

with correlation coefficients $0.63 < r < 0.69$ and $-0.75 < r < -0.63$ for the positive and negative correlations, respectively. In contrast, using $q = 0.05$ did not produce any result in the analysis with IRM. But, in the latter analysis, we found significant results for $q = 0.2$, with $p < 10^{-6}$, $0.59 < r < 0.69$ and $-0.72 < r < -0.59$.

The above results were summarised by counting the number of significant brain-wide connections. Specifically, Table 2 shows the outcome separately for the DRM and IRM tests, positive and negative correlations, and for each frequency band. Notice that the number of significant negative correlations was much more prominent for lower frequencies for both cognitive tests, whereas positive correlations were more prominent for higher frequencies. Interestingly, lower values of the cognitive tests are expected for participants showing a mild or advanced stage of dementia with respect to age-matched HC. Consequently, our results showed a significant relationship between increased FC strength and cognitive decline in the lower frequency bands, which has been previously interpreted as FC hypersynchronization (i.e. higher FC strength in MCI with respect to HC participants) and considered as related to cognitive decline (Engels et al., 2017; Garcia-Marin et al., 2009; Koelewijn et al., 2019; López et al., 2014).

Our results are also consistent with the notion that the DRM score seems to provide a more sensitive measure of cognitive decline than IRM and other tests (Welsh et al., 1991). As mentioned above, in contrast to the analysis with DRM, no significant associations were found for the analysis with IRM when FDR was applied with $q = 0.05$. Furthermore, both DRM and IRM scores exhibited very similar trend information, as the Spearman rank-correlation analysis between both scores produced an almost perfect relationship ($r = 0.94$, with negligible p-value). To some extent, this is also consistent with our previous analysis (albeit

using a different dataset) that showed a probabilistic causal relationship between immediate and delayed recall memory scores (Ding et al., 2018).

The results for both the DRM and IRM analyses were further explored by visual inspection of the high-dimensional FC maps for the significantly correlated connections (Fig. 3). In these maps we could clearly appreciate the increased details in contrast to traditional ROI-based approaches, which revealed the strongest correlations predominantly among the interactions of occipitofrontal, occipitotemporal and parietotemporal regions in the left hemisphere in δ band (Fig. 3A–B), and central and occipitotemporal regions in the left hemisphere in θ_2 band (Fig. 3C–D). Significant correlations were also exhibited by connections in the right hemisphere and between both hemispheres, but the latter networks seemed to be much less organized in comparison with the left-hemispheric connectivity. Furthermore, the substantial overlap of the FC cortical maps for both the DRM and IRM corroborated the above-mentioned tight relationship between DRM and IRM scores.

Next, we summarised our results using a parcellation of the cortical surface into ROIs only for comparison purposes with the literature. Specifically, we employed the Desikan-Killiany atlas (Desikan et al., 2006) and reported the significant inter-regional FC derived from the previous high-dimensional FC results. Fig. 4 shows a schema ball summarization of the correlation analysis between the FC and DRM scores for the more relevant interactions reported in Table 2. In this representation, the number of connections between any two ROIs was estimated as the number of significant connections between the ROI sources. As shown in each schema, this number was normalised with respect to the highest value within each representation.

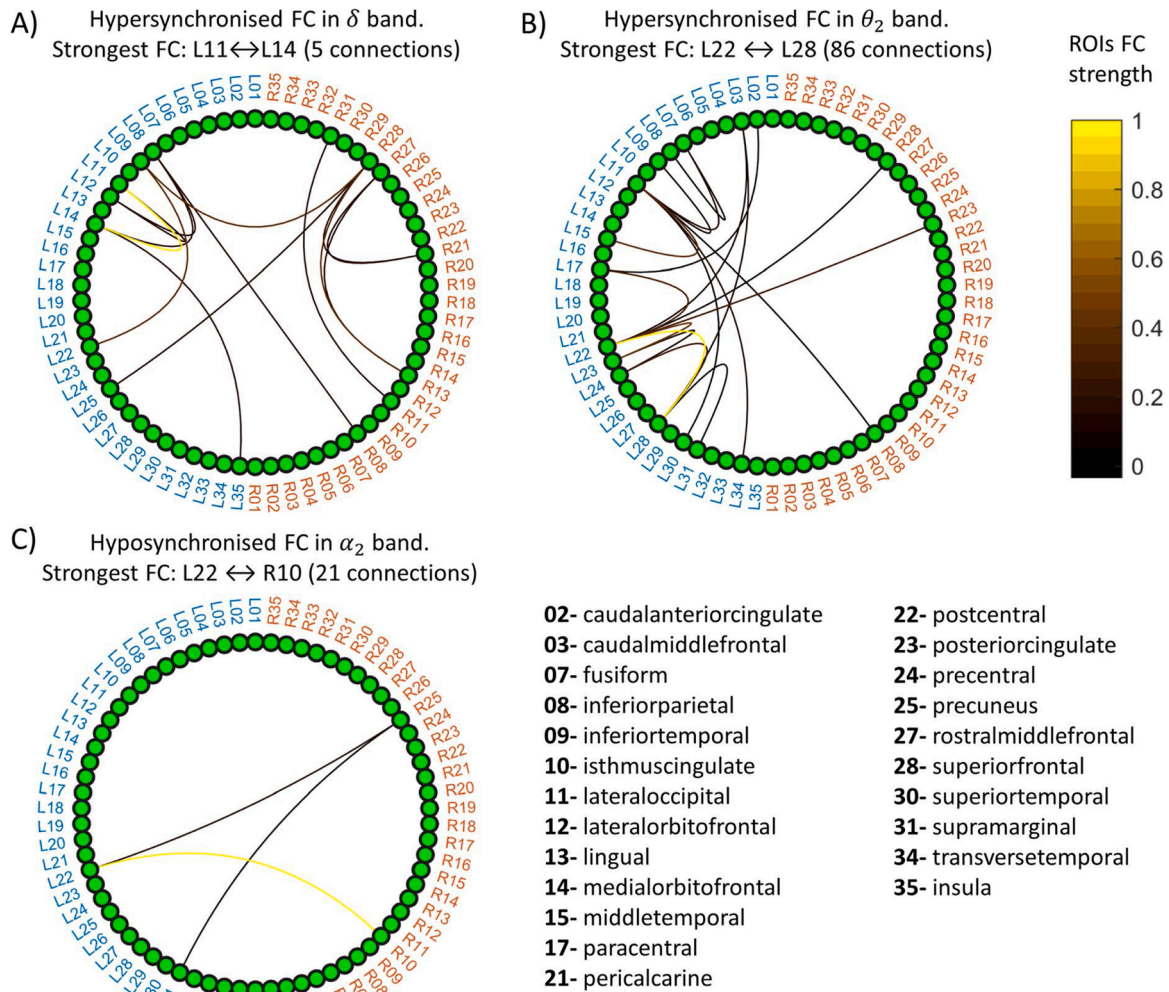


Fig. 4. Inter-regional FC significantly correlated with DRM score. The connectivity strength between two regions of the Desikan-Killiany atlas is estimated as the number of significant connections between the two regions in the corresponding high-dimensional correlation analysis. Region labels are shown separately for the left hemisphere (blue) and right hemisphere (red). The colormap indicates the inter-regional connectivity strength (values between 0 and 1), where this value is normalised as the number of connections divided by its highest value. (A–B) Graphs of hypersynchronised connectivity (FC strength significantly higher in MCI with respect to HC participants, $MCI >> HC$) as identified in δ and θ_2 frequency bands. All significant connections in these bands showed negative correlations (see Table 2). (C) Graph of hyposynchronised connectivity ($MCI << HC$) as identified in α_2 frequency band. All connections in this band showed positive correlations (see Table 2).

For the FC hypersynchronization, the most prominent associations were found between the lateral occipital and medial orbitofrontal regions in δ band (Fig. 4A, 5 connections between ROI #11 and ROI #14 in the left hemisphere, or L11 \leftrightarrow L14), and between the adjacent post-central and superior frontal regions in θ_2 band (Fig. 4B, L22 \leftrightarrow L28 with 86 connections). Otherwise, the most relevant hyposynchronisation (FC strength is decreased in MCI with respect to HC) was found between the left-hemispheric postcentral regions and right-hemispheric isthmus cingulate cortex in α_2 band (Fig. 4C, L22 \leftrightarrow R10 with 21 connections). Overall, these results are interesting per se and serve as comparison standards for the following analysis.

3.2. CPS analysis more consistently detects brain-wide communication

To recall, the proposed high-dimensional analyses involved about 0.27 billion features. Therefore, Bonferroni and FDR tests can be expected to produce conservative results. In this situation, it has been shown that the CPS could serve as a less conservative statistic since it can exploit the spatial structure in the data (Zalesky et al., 2012b, 2010). By clustering together spatially related features in combination with a

permutation approach that preserves the spatial structure, CPS can automatically reduce dimensionality while increasing the sensitivity of post-hoc statistical analyses. Here, the CPS was computed after defining suprathresholds corresponding to p-values $p_1 = 10^{-7}$, $p_2 = 10^{-6}$, and $p_3 = 10^{-5}$ for selecting relevant features at the lower and upper tails, separately, for the Wilcoxon rank-sum and the Spearman rank-correlation analysis.

In our study, the application of CPS produced significant results only for the rank-correlation analysis between FC and DRM scores in the θ_2 band, and for the rank-sum analysis (MCI vs. HC contrast) of FC strength in the δ band. For the former analysis, Fig. 5 shows the cortical FC maps of the whole set of connections surviving the pruning according to the defined suprathreshold p-values, ordered from the most (top) to less conservative (bottom) suprathresholds (Fig. 5A). Correspondingly, the distributions of the maximum-cluster-size statistic are shown in the middle column separately from top to bottom for each suprathreshold, together with the highlighted 95th percentile of the distribution which was selected as the critical value (Fig. 5B). Unsurprisingly, this value increased dramatically from more conservative (critical value CV = 59.0) to less conservative analysis (CV = 603.5). As stated previously

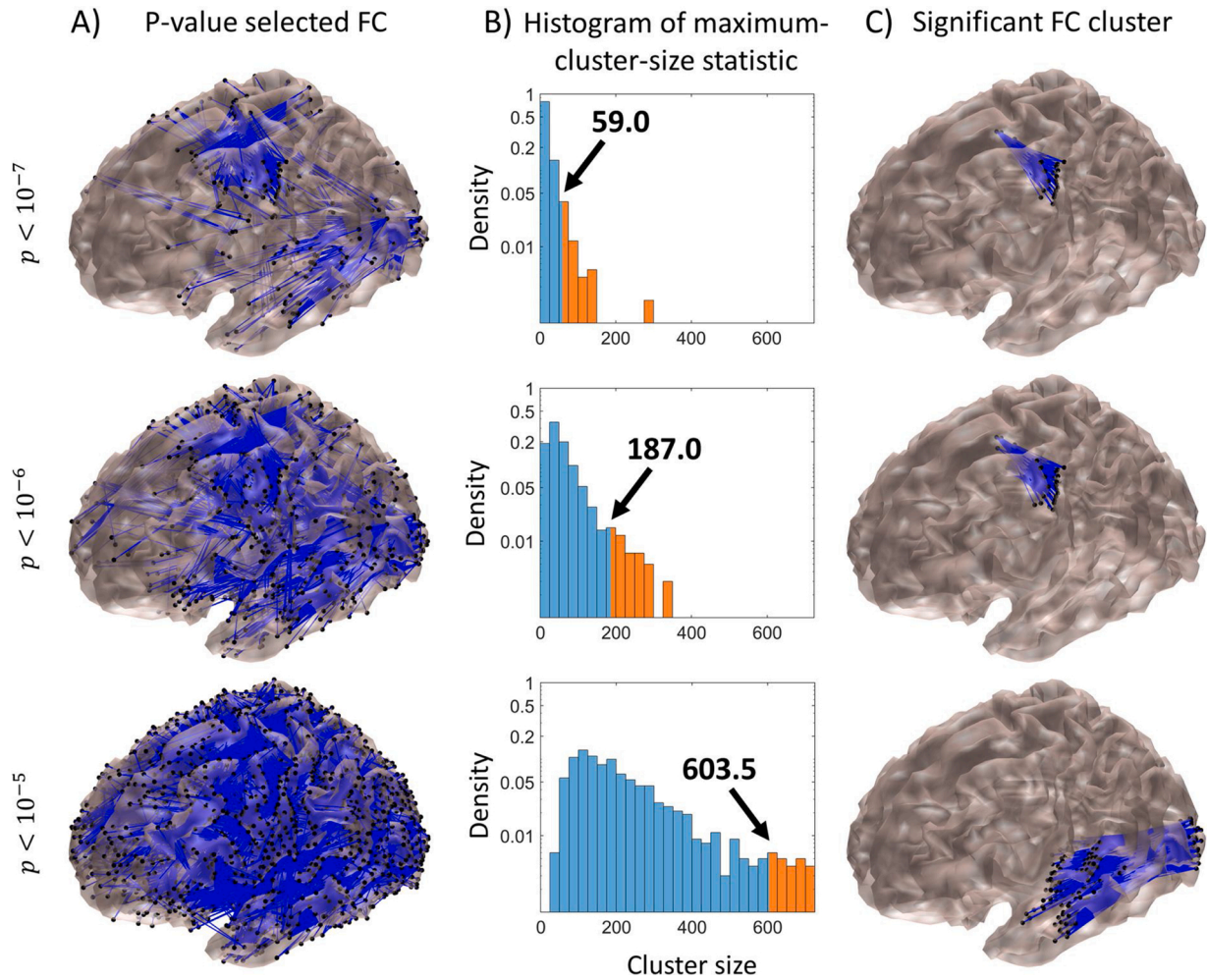


Fig. 5. Significant clusters detected using the cluster-permutation statistic for the Spearman rank-correlation analysis between FC strength and DRM score in θ_2 band. Three different suprathreshold values were tested as represented per row. (A) Cortical maps of all connections surviving after pruning for each suprathreshold value. (B) Normalised histograms of the probability distributions of the maximum-cluster-size statistic (horizontal-axis) with corresponding arrow-annotated 95th percentile, which is the critical value for selecting the significant clusters in the actual data. The distribution upper tail is highlighted in orange. The vertical axis represents the relative probability values in the range 0-1, shown in a log-scale for clear visibility. (C) Significant clusters that remain after removing the clusters with extension lower than the corresponding critical value.

Table 2

Number of significant FC links correlated with IRM and DRM scores. Positive and negative correlations are counted separately for each considered frequency band: 0.5-4 Hz (δ), 4-6 Hz (lower-theta, θ_1), 6-8 Hz (upper-theta, θ_2), 8-10.5 Hz (lower-alpha, α_1), 10.5-13 Hz (upper-alpha, α_2), 13-20 Hz (lower-beta, β_1), 20-30 Hz (upper-beta, β_2), and 30-48 Hz (gamma, γ). More relevant negative interactions were found in lower frequency bands, particularly δ and θ_2 bands (highlighted in blue colour in the online version), whereas more relevant positive interactions were found in higher frequency bands, particularly α_2 band (red colour).

	FC↔DRM correlation (FDR $q = 0.05$)								FC↔IRM correlation (FDR $q = 0.2$)							
	δ	θ_1	θ_2	α_1	α_2	β_1	β_2	γ	δ	θ_1	θ_2	α_1	α_2	β_1	β_2	γ
Positive	0	0	0	0	30	6	1	2	0	0	0	4	34	20	2	28
Negative	21	14	419	5	0	0	0	0	175	59	541	143	4	0	2	0

(Materials and Methods), only those clusters estimated from the actual data with extension exceeding the corresponding critical value were retained (Fig. 5C).

In Fig. 5C, notice that the same cluster with different extensions, involving the communication among the central regions, was significant for the more conservative suprathreshold values (top two rows). For the most conservative ($p_1 = 10^{-7}$), it survived with extension of 135

connections ($CV = 59.0$), whereas for a less conservative threshold ($p_2 = 10^{-6}$) it survived with extension of 227 connections ($CV = 187.0$). Interestingly, for the least conservative suprathreshold ($p_3 = 10^{-5}$) this cluster vanished completely while a different cluster with a much higher extension of 1019 connections survived ($CV = 603.5$). This latter cluster captured the communication between occipitotemporal regions in the left hemisphere (Fig. 5C, bottom). The above results were

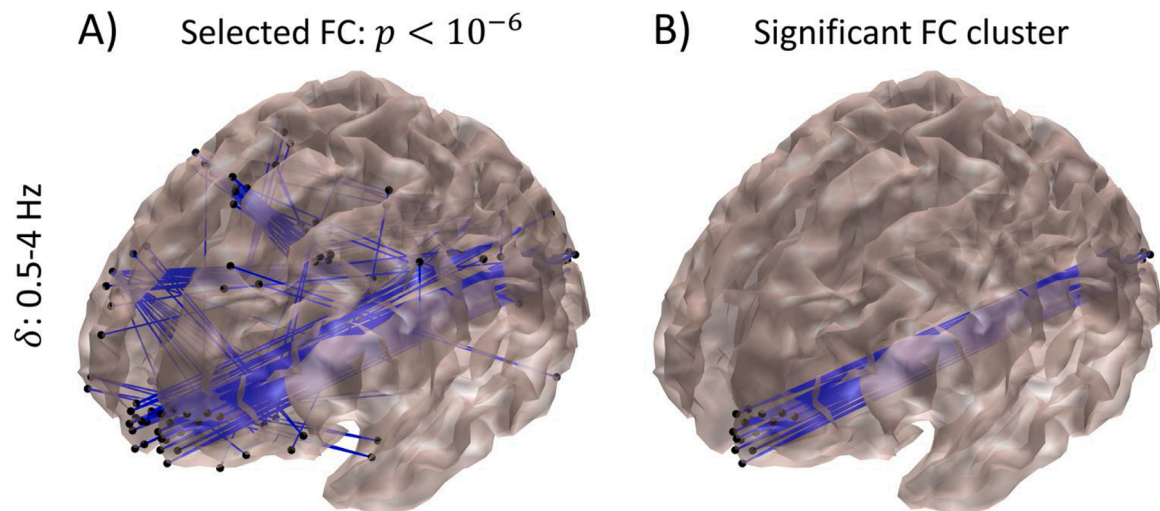


Fig. 6. Significant clusters detected using the cluster-permutation statistic for the Wilcoxon rank-sum analysis (MCI vs. HC) in δ band. (A) Connections surviving after pruning for a selected suprathreshold value (10^{-6}). (B) Only a cluster involving occipitotemporal regions (111 connections) survived after the correction by maximum-cluster-size statistics. See Fig. 5 caption for further details.

consistent with a previous observation that more conservative thresholds could reveal spatially focal clusters, whereas the lesser conservatives may reveal widely extended clusters (Friston et al., 1994; Zalesky et al., 2012a). Furthermore, note that these clusters involved hypersynchronized FC as the rank-correlation analysis between FC and DRM scores produced negative values ($-0.75 < r < -0.58$ for the bigger cluster of central regions, and $-0.69 < r < -0.53$ for the occipitotemporal cluster), indicating that the increased FC strength in these regions could be a sign of memory impairment.

For the rank-sum analysis in the δ band, we only found a single significant cluster of hypersynchronized FC (significantly increased FC in MCI with respect to HC participants) between occipitofrontal regions in the left hemisphere as shown in Fig. 6B. However, this cluster was only significant for $p_2 = 10^{-6}$, which shows that selecting an appropriate suprathreshold value may be a challenge. Furthermore, note that these connections were not observed when the same contrast was submitted for the FDR analysis in the previous sections, which could evidence that SPC produce more sensitive results. Interestingly, the connections in this cluster overlapped with the significant connections previously detected by the rank-correlation analysis between FC strength and DRM/IRM scores with the use of FDR, in the same frequency band (see Fig. 3A–B).

Similarly, a more detailed inspection of the significant clusters obtained in the rank-correlation analysis also revealed consistency between the FC clusters of central and occipitotemporal regions (Fig. 5C) with the significant connections obtained within the FDR analysis in the same frequency band (Fig. 3C–D). Overall, this suggested the significance of these interactions at both the cluster and individual connection levels in our study, albeit the finding of significant clusters offers a more solid proof for interregional communication.

3.3. Developing neuromarkers of cognitive dysfunctions with high-dimensional source-based MEG-FC and CPS analysis

Here, we first observe that our main results revealed the significant hypersynchronization of occipitotemporal and occipitofrontal networks, which could be associated with an ongoing AD pathology given the overlap with the critical regions affected during the early stages of AD progression according to Braak's staging system (Braak et al., 2006). Second, as a FC cluster more consistently connect two regions, a cluster-strength index could provide more critical information that may be useful for developing neuromarkers of cognitive decline.

Beforehand, the above significant networks derived by the CPS application were mapped into ROI connectivity maps using the Desikan-Killiany atlas. First, Fig. 7A (left) exposes the weight matrix for the cluster of central regions that was reported above (see Fig. 5C, middle row). This cluster revealed that the strongest interaction was observed between the postcentral and superior frontal regions (126 connections). Similarly, Fig. 7B (left) exposes the weight matrix for the regions in the occipitotemporal network (see Fig. 5C, bottom row), where the strongest association was found between the lateral occipital area with the middle, superior, and transverse temporal regions with 340, 350 and 139 connections, respectively. Finally, Fig. 7C (left) exposes the weight matrix for the cluster of occipitofrontal connections (see Fig. 6B), in which the strongest FC was found between the lateral occipital region with the lateral and medial orbitofrontal regions, with 25 and 69 connections, respectively. These brain regions are known to be critical for memory, emotion, object and face processing, which are among the principal cognitive functions affected during AD progression (Desgranges et al., 1998; Grill-Spector et al., 2001; Kringelbach and Rolls, 2004; Rolls, 1999; Serrano-Pozo et al., 2011).

To evaluate whether these clusters could be used to predict cognitive decline, we first proceeded to average all the cluster connections to produce a single-valued cluster-strength index, separately for each cluster and participant, i.e. averaging the 227, 1019 and 111 connections, corresponding to the central (Fig. 7A), occipitotemporal (Fig. 7B) and occipitofrontal (Fig. 7C) clusters. Subsequently, we evaluated the predictive value for the first two clusters using receiver operating characteristic (ROC) analysis. For simplicity, we provided the classification targets (HC or MCI) and the cluster-strength index as parameters for estimating the ROC curves, together with their corresponding 95 % confidence interval (CI) and area under curve (AUC) values, using $N = 1000$ bootstrap replications. We found that the cluster-strength index showed a high classification performance with $AUC = 0.81$, $CI = [0.69; 0.90]$, and $AUC = 0.79$, $CI = [0.65; 0.89]$, for the corresponding clusters (Fig. 7A–B, right-side column). For the third cluster, we conducted Spearman rank-correlation analysis between its cluster-strength index and DRM test scores, which revealed a strong negative correlation with $r = -0.67$ and $p < 10^{-8}$ (Fig. 7C, right-side column), which reinforces the observation that FC hypersynchronization could be an early sign of cognitive decline.

We note that the first two clusters cannot be used in the latter analysis, nor the third cluster can be used in the former analysis, without incurring in statistical circularity. Overall, these results demonstrate the

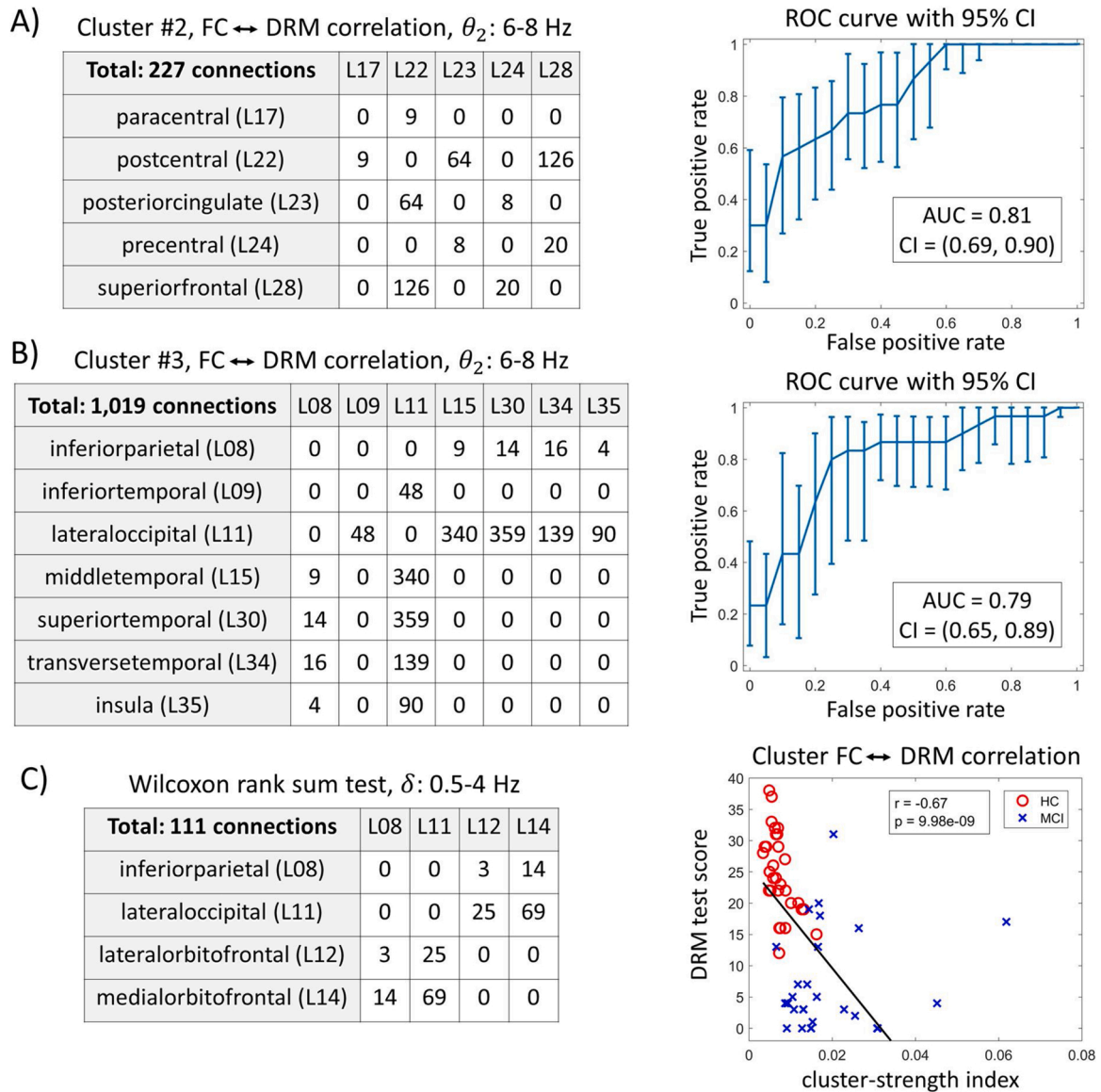


Fig. 7. Biomarker evaluation of cluster-strength index for prediction of cognitive decline. (A-C) Clusters derived from Spearman rank-correlation and Wilcoxon rank-sum analyses are further scrutinised (cluster FC maps were plotted in Fig. 5C, middle and bottom row, and Fig. 6B, correspondingly in the same order). For each cluster, interregional weight connectivity matrices were obtained by counting the number of significant connections between two different regions of the Desikan-Killiany atlas, while a cluster-strength index was estimated as the average of all the cluster FC values, separately for each participant. Note that each cluster only connects a small number of ROIs as shown in the matrices. **A** (left-side column): the first cluster mostly connects postcentral with posterior cingulate and adjacent superior frontal regions. **B** (left-side column): the second cluster contains a hub located in the lateral occipital cortex, with a significant number of connections to inferior, middle, superior, and transverse temporal gyrus, and insula. **C** (left-side column): the third cluster mostly connects lateral occipital with lateral and medial orbitofrontal cortex. **A-C** (right-side column): an estimated cluster-strength index is used to evaluate cognitive decline. **A-B** (right-side column): for the first two clusters separately, ROC analysis is performed using the cluster-strength index and the corresponding HC/MCI label for each participant, which includes the estimation of its 95 % confidence interval and area under the curve (AUC) statistic. **C** (right-side column): for the third and last cluster, Spearman rank-sum correlation analysis was conducted between the cluster-strength index and DRM test scores. Red open circle: HC participant; blue cross: MCI.

high predictive value and sensitivity of using a cluster-strength index, despite the simplicity of using just a single feature in our analysis. Therefore, it may provide an optimistic prospect for the development of a source MEG-FC neuromarker in AD research.

4. Discussion

To the best of our knowledge, this is the first time that M/EEG analyses have been conducted on such a large scale with about 0.27 billion features. In the typical studies, FC analyses are often limited to the use of coarse brain regional parcellation, falling short of fully exploiting the ample information of the original data (Engels et al., 2017; Hillebrand

et al., 2012; Raichle, 2015; van den Heuvel and Hulshoff Pol, 2010; Zalesky et al., 2010), and thus leading to information loss, reduced statistical sensitivity, and consequently to potential bias in research findings (Hillebrand et al., 2012; Zalesky et al., 2012b). To avoid such limitations, here we studied the estimation and statistical mapping of brain FC with its intrinsic high-dimensional characteristics, using a robust FC measure (Sanchez-Bornot et al., 2018) and a proposed unified framework for cluster-permutation statistical (CPS) analysis (see Materials and Methods). We demonstrated our approach with the use of source-based MEG-FC analysis using a database of 30 HC and 30 MCI participants that also included neuropsychological data. The MCI participants had memory impairment and hippocampal atrophy as detected

by structural MRI scans (see Table 1), thereby the MCI can be linked to AD pathology with an intermediate likelihood (Albert et al., 2011). We consider that this application is of utmost importance to show the prospect of source MEG-FC analysis for studying neuromarkers of Alzheimer's disease (AD) and its earlier progression.

4.1. Significance of high-dimensional MEG-FC analysis using CPS

As an important contribution, we proposed a unified framework for CPS analysis (Zalesky et al., 2012b, 2012a, 2010; Zhang et al., 2018) to make possible our study involving a huge number of connections in source MEG-FC analysis. This was realised by observing that the essential difference between the network-based statistic (NBS) (Zalesky et al., 2010) and the spatial pairwise clustering (SPC) (Zalesky et al., 2012a) is in the considered neighbourhood criterion to evaluate adjacent connections (see Fig. 1). Additionally, we introduced here a novel neighbourhood measure that was discussed in detail for the CPS analysis of high-dimensional FC maps in the brain cortical surface (see Materials and Methods). Our approach was unlike previous studies that used FC analysis or cluster-permutation statistic in a reduced space, by: (i) conducting the analysis among the sources of selected regions based on prior information (Mamashli et al., 2019); (ii) analysing significant connected components (Zalesky et al., 2010); (iii) considering the connectivity mapping of a seed point within the brain (Hipp et al., 2012); or (iv) using coarser grids to avoid the possible spurious estimation of FC among nearby sources (Zalesky et al., 2012b, 2012a). In contrast, we have used most of the available information in a source MEG-FC manifold to render less-biased conclusions.

Note that Zalesky et al. (2012a) observed that the use of NBS could be preferable for coarser spatial resolution, whereas the SPC could be superior in higher resolution (see Fig. 3 in Zalesky et al., 2012a, and discussion therein), where the latter could be explained by observing that SPC's neighbourhood criterion is more restrictive than NBS's. Following the same reasoning, we observed that our novel neighbourhood measure is more restrictive than the SPC's (see Fig. 1), thus the significance testing of salient clusters could be more robust with our measure than with previous methods only in analysis with very high spatial resolution. Although we do not perform any comparison analysis among the different neighbourhood measures, it can be clearly appreciated the compactness of significant clusters detected in our study with our proposed measure (see Figs. 5,6).

Importantly, our work has shown that CPS analysis can be performed in very high-dimensional scenarios without much computational burden (see Materials and Methods). Furthermore, it should be noted that CPS controls the family-wise error rate by testing significance at the cluster instead of individual connections (Hayasaka and Nichols, 2003; Zalesky et al., 2012b, 2012a, 2010). Therefore, when performing source MEG-FC analyses with CPS, we focused on the significant detected FC clusters and proposed a cluster-strength index. Not only our significant clusters revealed critical networks involved in memory and cognitive processing (Figs. 5,6), our cluster-strength index also showed promising results in evaluating the cognitive status of the participants (Fig. 7).

4.2. Implementing CPS analysis in high-dimensional scenarios

We refuted a pessimistic observation made in the SPC paper (Zalesky et al., 2012a), where the authors stated that the cluster partition of suprathreshold connections is "performed by initializing an $N(N-1)/2 \times N(N-1)/2$ adjacency matrix", which will be unfeasible in our case with $N = 8196$ sources. As has been shown here, our testing of a neighbourhood relationship between two connections exclusively rely on the testing of a neighbourhood relationship in the cortical surface (see Materials and Methods and Supp. Fig. 3). Therefore, if we use an adjacency matrix to reflect this relation, our matrix will be of dimensions $N \times N$, which is a huge improvement with respect to the previous observation. Alternatively, using a sparse matrix

representation or a list data-structure for keeping track of the neighbouring vertices of each vertex will translate into additional computational gains.

In our proposed implementation of the CPS analysis, the permutation and statistical procedures were performed separately (blockwise) for each of the $C_2^{17} = 136$ sub-blocks (16×16 partition) of the strictly upper-part of a triangular FC matrix ($8196 \times 8195/2$ pairwise connections) and defined frequency bands (Materials and Methods). If users have a lower RAM memory capacity, a finer sub-blocks partition should be considered, e.g. a 41×41 partition (40 blocks times 200 sources + 1 block times 196 sources = 8196) for a total of $C_2^{42} = 861$ sub-blocks. This blockwise approach helps to make more feasible the implementation of CPS analyses, reducing the RAM use to the memory requirement for each block computations.

Furthermore, note that saving only the indices for the suprathreshold features allowed a very sparse representation of the large-scale FC matrices for the different frequency bands, as only those features corresponding to the selected suprathreshold values $p_1 = 10^{-7}$, $p_2 = 10^{-6}$, and $p_3 = 10^{-5}$, separately, were considered for the subsequent cluster analysis. Therefore, the expected density of derived FC matrices is in the same order. Summing up, despite having about 0.27 billion features and running up to 1000 Monte Carlo simulations in our study, the implementation of the CPS framework was possible because of the mentioned high sparsity, blockwise strategy and other novel computational ideas (see Materials and Methods).

4.3. ROI vs large-scale brain-wide based FC analysis

It would have been possible to conduct sensor-level M/EEG-FC analyses (Engels et al., 2017) with CPS, with the advantages that the number of sensors is considerably smaller than the number of sources. As nearby sensors record similar oscillations emanating from the underlying neuronal population, it is appropriate to use cluster statistics to exploit the smooth spatial FC patterns. However, a sensor can also identify significant activity from multiple sources located at distant sites, thus hindering the results interpretation. Less negative issues occur when using ROI-based source FC analyses. One extreme case is when the ROIs are coarsely defined by the brain lobes, in which case it resembles the sensor-level analysis. At the other extreme, FC analyses based on a very fine ROI parcellation (Craddock et al., 2012; Glasser et al., 2016) could produce results comparable with those using a high-dimensional approach.

However, despite the observation that ROI analysis may provide robustness against inter-individual functional and anatomical variability (Hillebrand et al., 2012), it certainly leads to loss of information with the associated degraded sensitivity of post-hoc statistical analyses and biased results (Hillebrand et al., 2012; Zalesky et al., 2012a, 2010). In contrast, our approach uses most of the available information in a high-dimensional manifold while dealing with volume conduction in source FC analysis (Sanchez-Bornot et al., 2018). Furthermore, the inter-individual variability is controlled in our approach due to the characteristic spatial blurriness of estimated source activities (Mattout et al., 2006), which may be conveyed to the FC analysis, without incurring in any a-priori compromise on a particular brain region parcellation. Altogether, CPS analysis may lead to increased robustness of FC mapping, where discovered FC clusters should more confidently represent the actual brain networks.

In contrast to ROI analysis, the use of large-scale brain-wide FC approach also allows for direct comparisons with ECoG analysis to measure FC in the brain (Hipp et al., 2012; Wang et al., 2019). Particularly, with the use of the EIC method or an imaginary coherence index (Nolte et al., 2004; Sanchez-Bornot et al., 2018), which are robust to volume conduction, we ameliorate the risk that the measured interactions are spurious and allow for the robust estimation of short-range connectivity in the brain. Critically, EIC can also measure

true interactions caused by zero-lag (modulus π) phase interactions that are neglected by other imaginary coherence measures (Sanchez-Bornot et al., 2018), which is an advantage inherited by our high-dimensional FC approach.

4.4. Prospective neuromarker importance of source MEG-FC analysis

Consistent with our findings (Figs. 3–7 and Table 2), the state-of-the-art in AD research using M/EEG data have established a relationship between hypersynchronized FC and memory decline (Dimitriadis et al., 2018; Engels et al., 2017; Koelewijn et al., 2019; López et al., 2014; Maestú et al., 2015). Particularly, our high-dimensional FC analyses exposed significant hypersynchronized communication of occipito-temporal and occipitofrontal regions (Fig. 7, left-side column). Such hypersynchronization phenomenon could be attributed to overall neuronal excitatory enhancement (Zou et al., 2012), reduced disinhibition of neurons (Garcia-Marin et al., 2009), or as a compensatory mechanism related to brain plasticity changes triggered by AD synaptic and neuronal loss (Frere and Slutsky, 2018; Styr and Slutsky, 2018).

Among the significantly found connected regions, there is a consensus that the insula and temporal areas (e.g. transverse temporal, Fig. 7B) are critically involved in episodic memory processes (Desgranges et al., 1998; Serrano-Pozo et al., 2011). Other significantly connected regions in the frontal (lateral and medial orbitofrontal cortex), lateral occipital, and inferior parietal cortices (Fig. 7C), are important for decision making, reward evaluation, face/object and emotion processing (Grill-Spector et al., 2001; Kringelbach and Rolls, 2004; Rolls, 1999).

Furthermore, our main results (Figs. 5–7) overlapped with previously reported hypersynchronization in similar brain regions (Dimitriadis et al., 2018; Engels et al., 2017; Yu et al., 2017). Although, in our case, the identification of significant FC clusters provides stronger evidence for this claim, as clusters can more robustly support the evidence of inter-regional communication in contrast to the sparse FC patterns exposed in previous works (Dimitriadis et al., 2018; Engels et al., 2017; Hillebrand et al., 2012; Koelewijn et al., 2019; Yu et al., 2017), with the additional advantage that the smooth characteristic of FC clusters also brings robustness against inter-individual anatomical and functional variability. Therefore, we suggest that these two properties of FC clusters are important for a source MEG-FC neuromarker in dementia. Here, we further supported the importance of cluster analysis by showing that a cluster-strength index could be used to evaluate cognitive decline with promising results (Fig. 7, right-side column). However, note that these results must be interpreted with caution because the limited sample size in our study. Thus, our results must be further scrutinised using different databases in future studies.

4.5. Concluding remarks

Our high-dimensional FC measure is resilient to the negative effects of the instantaneous propagation of the brain electromagnetic activity or volume conduction, which can result in the discovery of spurious FC (Nolte et al., 2004; Sanchez-Bornot et al., 2018). Therefore, our approach is very appropriate to study both short- and long-range interactions in the brain. Note also that artifact signals such as those emanating from eye movements, heartbeat and muscular artifacts can produce spurious FC due to volume conduction, indicating that artifact removal should be made mandatory to avoid this danger. However, against this logic, it has been indicated that a FC measure which is robust to volume conduction must also be resilient to this side effect of the artifact signals (Hillebrand et al., 2012). Moreover, as removing artifacts signals from M/EEG recordings can also delete neural activity components of interest and harm subsequent analyses (Thompson et al., 2019; Winkler et al., 2014), then using a robust FC measure could become a practical choice for using on the raw data, as shown in our study. Because the importance of these observations, we recommend to further

investigate it in future studies while providing preliminary results in the Supplementary Materials (see Supp. Figs. 5–6 and discussion therein) to support our analysis.

Overall, we have successfully developed an analytical pipeline involving a unified CPS framework for analysing high-dimensional brain-wide FC maps, while avoiding the biases that come along with standard brain parcellation approaches. Such high-resolution FC maps can be estimated without high computational cost and could become important to advance research in healthy and unhealthy neural information processing. Our proposed approach can, in general, be applied to a variety of neuroimaging studies, including translational clinical research.

CRedit authorship contribution statement

Jose M. Sanchez-Bornot: Conceptualization, Methodology, Software, Validation, Formal analysis, Investigation, Writing - original draft, Writing - review & editing, Visualization. **Maria E. Lopez:** Formal analysis, Investigation, Data curation, Writing - review & editing. **Ricardo Bruña:** Validation, Writing - review & editing. **Fernando Maestu:** Writing - review & editing, Supervision. **Vahab Youssofzadeh:** Validation, Writing - review & editing. **Su Yang:** Validation, Writing - review & editing. **David P. Finn:** Writing - review & editing, Funding acquisition. **Stephen Todd:** Writing - review & editing, Funding acquisition. **Paula L. McLean:** Writing - review & editing, Project administration, Funding acquisition. **Girijesh Prasad:** Writing - review & editing, Project administration, Funding acquisition. **KongFatt Wong-Lin:** Conceptualization, Methodology, Writing - original draft, Writing - review & editing, Supervision, Project administration, Funding acquisition.

Declaration of Competing Interest

None.

Acknowledgments

This work was supported by the EU's INTERREG VA Programme, managed by the Special EU Programmes Body (SEUPB) (J.M.S.-B., P.L.M. and K.W.-L.), the Northern Ireland Functional Brain Mapping Project (1303/101154803) funded by Invest NI and Ulster University (S.Y., G.P. and K.W.-L.), the Spanish Ministry of Economy and Competitiveness (PSI2009-14415-C03-01) and Madrid Neurocenter (M.E.L., R.B. and F.M.), Alzheimer's Research UK (ARUK) Pump Priming Awards (D.P.F., S.T., G.P., P.L.M. and K.W.-L.), and Medical College of Wisconsin (V.Y.). P.M. and K.W.-L. received additional support from Ulster University Research Challenge Fund, and Global Challenges Research Fund, and K.W.-L. from COST Action Open Multiscale Systems Medicine (Open-MultiMed) supported by COST (European Cooperation in Science and Technology). The views and opinions expressed in this paper do not necessarily reflect those of the European Commission or the Special EU Programmes Body (SEUPB).

Appendix A. Supplementary data

Supplementary material related to this article can be found, in the online version, at doi:<https://doi.org/10.1016/j.jneumeth.2020.108991>.

References

- Albert, M.S., DeKosky, S.T., Dickson, D., Dubois, B., Feldman, H.H., Fox, N.C., Gamst, A., Holtzman, D.M., Jagust, W.J., Petersen, R.C., Snyder, P.J., Carrillo, M.C., Thies, B., Phelps, C.H., 2011. The diagnosis of mild cognitive impairment due to Alzheimer's disease: recommendations from the National Institute on Aging-Alzheimer's Association workgroups on diagnostic guidelines for Alzheimer's disease. *Alzheimer's Dement.* 7, 270–279. <https://doi.org/10.1016/j.jalz.2011.03.008>.

- Braak, H., Alafuzoff, I., Arzberger, T., Kretschmar, H., Tredici, K., 2006. Staging of Alzheimer disease-associated neurofibrillary pathology using paraffin sections and immunocytochemistry. *Acta Neuropathol.* 112, 389–404. <https://doi.org/10.1007/s00401-006-0127-z>.
- Buckner, R.L., Sepulcre, J., Talukdar, T., Krienen, F.M., Liu, H., Hedden, T., Andrews-Hanna, J.R., Sperling, R.A., Johnson, K.A., 2009. Cortical hubs revealed by intrinsic functional connectivity: mapping, assessment of stability, and relation to Alzheimer's disease. *J. Neurosci.* 29, 1860–1873. <https://doi.org/10.1523/JNEUROSCI.5062-08.2009>.
- Buckner, R.L., Krienen, F.M., Yeo, B.T.T., 2013. Opportunities and limitations of intrinsic functional connectivity MRI. *Nat. Neurosci.* 16, 832–837. <https://doi.org/10.1038/nn.3423>.
- Craddock, R.C., James, G.A., Holtzheimer, P.E., Hu, X.P., Mayberg, H.S., 2012. A whole brain fMRI atlas generated via spatially constrained spectral clustering. *Hum. Brain Mapp.* 33, 1914–1928. <https://doi.org/10.1002/hbm.21333>.
- de Vos, F., Koini, M., Schouten, T.M., Seiler, S., van der Grond, J., Lechner, A., Schmidt, R., de Rooij, M., Rombouts, S.A.R.B., 2018. A comprehensive analysis of resting state fMRI measures to classify individual patients with Alzheimer's disease. *Neuroimage* 167, 62–72. <https://doi.org/10.1016/j.neuroimage.2017.11.025>.
- Desgranges, B., Baron, J.C., de la Sayette, V., Petit-Taboué, M.C., Benali, K., Landeau, B., Lechevalier, B., Eustache, F., 1998. The neural substrates of memory systems impairment in Alzheimer's disease. A PET study of resting brain glucose utilization. *Brain* 121 (Pt 4), 611–631. <https://doi.org/10.1093/brain/121.4.611>.
- Desikan, R.S., Ségonne, F., Fischl, B., Quinn, B.T., Dickerson, B.C., Blacker, D., Buckner, R.L., Dale, A.M., Maguire, R.P., Hyman, B.T., Albert, M.S., Killiany, R.J., 2006. An automated labeling system for subdividing the human cerebral cortex on MRI scans into gyral based regions of interest. *Neuroimage* 31, 968–980. <https://doi.org/10.1016/j.neuroimage.2006.01.021>.
- Dimitriadis, S.I., López, M.E., Bruña, R., Cuesta, P., Marcos, A., Maestú, F., Pereda, E., 2018. How to build a functional connectomic biomarker for mild cognitive impairment from source reconstructed MEG Resting-state activity: the combination of ROI representation and connectivity estimator matters. *Front. Neurosci.* 12, 1–21. <https://doi.org/10.3389/fnins.2018.00306>.
- Ding, X., Bucholz, M., Wang, Haiying, Glass, D.H., Wang, Hui, Clarke, D.H., Bjourson, A. J., Roy, L., Dowey, C., O' Kane, M., Prasad, G., Maguire, L., Wong-Lin, K., 2018. A hybrid computational approach for efficient Alzheimer's disease classification based on heterogeneous data. *Sci. Rep.* 8, 9774. <https://doi.org/10.1038/s41598-018-27997-8>.
- Engels, M.M.A., van der Flier, W.M., Stam, C.J., Hillebrand, A., Scheltens, P., van Straaten, E.C.W., 2017. Alzheimer's disease: the state of the art in resting-state magnetoencephalography. *Clin. Neurophysiol.* 128, 1426–1437. <https://doi.org/10.1016/j.clinph.2017.05.012>.
- Frere, S., Slutsky, I., 2018. Alzheimer's disease: from firing instability to homeostasis network collapse. *Neuron* 97, 32–58. <https://doi.org/10.1016/j.neuron.2017.11.028>.
- Friston, K.J., Worsley, K.J., Frackowiak, R.S.J., Mazziotta, J.C., Evans, A.C., 1994. Assessing the significance of focal activations using their spatial extent. *Hum. Brain Mapp.* 1, 210–220. <https://doi.org/10.1002/hbm.460010306>.
- García-Marín, V., Blázquez-Llorca, L., Rodríguez, J.-R., Boluda, S., Muntane, G., Ferrer, I., Defelipe, J., 2009. Diminished perisomatic GABAergic terminals on cortical neurons adjacent to amyloid plaques. *Front. Neuroanat.* 3, 28. <https://doi.org/10.3389/neuro.05.028.2009>.
- Genovese, C.R., Lazar, N.A., Nichols, T., 2002. Thresholding of statistical maps in functional neuroimaging using the false discovery rate. *Neuroimage* 15, 870–878. <https://doi.org/10.1006/nimg.2001.1037>.
- Glasser, M.F., Coalson, T.S., Robinson, E.C., Hacker, C.D., Harwell, J., Yacoub, E., Ugurbil, K., Andersson, J., Beckmann, C.F., Jenkinson, M., Smith, S.M., Van Essen, D. C., 2016. A multi-modal parcellation of human cerebral cortex. *Nature* 536, 171–178. <https://doi.org/10.1038/nature18933>.
- Greicius, M.D., Krasnow, B., Reiss, A.L., Menon, V., 2003. Functional connectivity in the resting brain: a network analysis of the default mode hypothesis. *Proc. Natl. Acad. Sci. U.S.A.* 100, 253–258. <https://doi.org/10.1073/pnas.0135058100>.
- Greicius, M.D., Srivastava, G., Reiss, A.L., Menon, V., 2004. Default-mode network activity distinguishes Alzheimer's disease from healthy aging: Evidence from functional MRI. *Proc. Natl. Acad. Sci.* 101, 4637–4642. <https://doi.org/10.1073/pnas.0308627101>.
- Grill-Spector, K., Kourtzi, Z., Kanwisher, N., 2001. The lateral occipital complex and its role in object recognition. *Vision Res.* 41, 1409–1422. [https://doi.org/10.1016/S0042-6989\(01\)00073-6](https://doi.org/10.1016/S0042-6989(01)00073-6).
- Haak, K.V., Marquand, A.F., Beckmann, C.F., 2018. Connectopic mapping with resting-state fMRI. *Neuroimage* 170, 83–94. <https://doi.org/10.1016/j.neuroimage.2017.06.075>.
- Hayasaka, S., Nichols, T.E., 2003. Validating cluster size inference: random field and permutation methods. *Neuroimage* 20, 2343–2356. <https://doi.org/10.1016/j.neuroimage.2003.08.003>.
- Henson, R.N., Mattout, J., Phillips, C., Friston, K.J., 2009. Selecting forward models for MEG source-reconstruction using model-evidence. *Neuroimage* 46, 168–176. <https://doi.org/10.1016/j.neuroimage.2009.01.062>.
- Henson, R.N., Flandin, G., Friston, K.J., Mattout, J., 2010. A parametric empirical bayesian framework for fMRI-constrained MEG/EEG source reconstruction. *Hum. Brain Mapp.* 31, 1512–1531. <https://doi.org/10.1002/hbm.20956>.
- Hillebrand, A., Barnes, G.R., Bosboom, J.L., Berendse, H.W., Stam, C.J., 2012. Frequency-dependent functional connectivity within resting-state networks: an atlas-based MEG beamformer solution. *Neuroimage* 59, 3909–3921. <https://doi.org/10.1016/j.neuroimage.2011.11.005>.
- Hipp, J.F., Hawellek, D.J., Corbetta, M., Siegel, M., Engel, A.K., 2012. Large-scale cortical correlation structure of spontaneous oscillatory activity. *Nat. Neurosci.* 15, 884–890. <https://doi.org/10.1038/nn.3101>.
- Hollander, M., Wolfe, D.A., Chicken, E., 2013. *Nonparametric Statistical Methods*, Vol. 751. John Wiley & Sons.
- Koelewin, L., Lancaster, T.M., Linden, D., Dima, D.C., Routley, B.C., Magazzini, L., Barawi, K., Brindley, L., Adams, R., Tansey, K.E., Bompas, A., Tales, A., Bayer, A., Singh, K., 2019. Oscillatory hyperactivity and hyperconnectivity in young APOE-ε4 carriers and hypoconnectivity in Alzheimer's disease. *Elife* 8, 1–25. <https://doi.org/10.7554/elife.36011>.
- Kringelbach, M.L., Rolls, E.T., 2004. The functional neuroanatomy of the human orbitofrontal cortex: evidence from neuroimaging and neuropsychology. *Prog. Neurobiol.* 72, 341–372. <https://doi.org/10.1016/j.pneurobio.2004.03.006>.
- Litvak, V., Mattout, J., Kiebel, S., Phillips, C., Henson, R., Kilner, J., Barnes, G., Oostenveld, R., Daunizeau, J., Flandin, G., Penny, W., Friston, K., 2011. EEG and MEG data analysis in SPM8. *Comput. Intell. Neurosci.* 2011. <https://doi.org/10.1155/2011/852961>.
- Lobo, A., Escobar, V., Ezquerro, J., Seva Díaz, A., 1980. El Mini-Examen Cognoscitivo (Un test sencillo, práctico, para detectar alteraciones intelectuales en pacientes psiquiátricos). *Rev. Psiquiatr. y Psicol. Médica*.
- Logothetis, N.K., 2008. What we can do and what we cannot do with fMRI. *Nature* 453, 869–878. <https://doi.org/10.1038/nature06976>.
- López, M.E., Bruña, R., Aurtente, S., Pineda-pardo, J.Á., Marcos, A., Arrazola, J., Reinoso, A.I., Montejo, P., Bajo, R., Maestú, F., 2014. Alpha-band hypersynchronization in progressive mild cognitive impairment: a magnetoencephalography study. *J. Neurosci.* 34, 14551–14559.
- Maestú, F., Peña, J.M., Garcés, P., González, S., Bajo, R., Bagic, A., Cuesta, P., Funke, M., Mäkelä, J.P., Menasalvas, E., Nakamura, A., Parkkonen, L., López, M.E., Del Pozo, F., Sudre, G., Zamrini, E., Pekkonen, E., Henson, R.N., Becker, J.T., 2015. A multicenter study of the early detection of synaptic dysfunction in Mild Cognitive Impairment using Magnetoencephalography-derived functional connectivity. *Neuroimage Clin.* 9, 103–109. <https://doi.org/10.1016/j.nicl.2015.07.011>.
- Mamashli, F., Hämäläinen, M., Ahveninen, J., Kenet, T., Khan, S., 2019. Permutation statistics for connectivity analysis between regions of interest in EEG and MEG data. *Sci. Rep.* 9, 7942. <https://doi.org/10.1038/s41598-019-44403-z>.
- Maris, E., Oostenveld, R., 2007. Nonparametric statistical testing of EEG- and MEG-data. *J. Neurosci. Methods* 164, 177–190. <https://doi.org/10.1016/j.jneumeth.2007.03.024>.
- Mattout, J., Phillips, C., Penny, W.D., Rugg, M.D., Friston, K.J., 2006. MEG source localization under multiple constraints: an extended Bayesian framework. *Neuroimage* 30, 753–767. <https://doi.org/10.1016/j.neuroimage.2005.10.037>.
- Mattout, J., Henson, R.N., Friston, K.J., 2007. Canonical source reconstruction for MEG. *Comput. Intell. Neurosci.* 2007. <https://doi.org/10.1155/2007/67613>.
- Nolte, G., Bai, O., Wheaton, L., Mari, Z., Vorbach, S., Hallett, M., 2004. Identifying true brain interaction from EEG data using the imaginary part of coherency. *Clin. Neurophysiol.* 115, 2292–2307. <https://doi.org/10.1016/j.clinph.2004.04.029>.
- O'Neill, G.C., Tewarie, P., Vidaurre, D., Luzzi, L., Woolrich, M.W., Brookes, M.J., 2018. Dynamics of large-scale electrophysiological networks: a technical review. *Neuroimage* 180, 559–576. <https://doi.org/10.1016/j.neuroimage.2017.10.003>.
- Oldfield, R.C., 1971. The assessment and analysis of handedness: The Edinburgh inventory. *Neuropsychologia* 9, 97–113. [https://doi.org/10.1016/0028-3932\(71\)90067-4](https://doi.org/10.1016/0028-3932(71)90067-4).
- Power, J.D., Cohen, A.L., Nelson, S.M., Wig, G.S., Barnes, K.A., Church, J.A., Vogel, A.C., Laumann, T.O., Miezin, F.M., Schlaggar, B.L., Petersen, S.E., 2011. Functional network organization of the human brain. *Neuron* 72, 665–678. <https://doi.org/10.1016/j.neuron.2011.09.006>.
- Raichle, M.E., 2015. The brain's default mode network. *Annu. Rev. Neurosci.* 38, 433–447. <https://doi.org/10.1146/annurev-neuro-071013-014030>.
- Reisberg, B., Ferris, S.H., de León, M.J., Crook, T., 1982. The Global Deterioration Scale for assessment of primary degenerative dementia. *Am. J. Psychiatry* 139, 1136–1139. <https://doi.org/10.1176/ajp.139.9.1136>.
- Rolls, E.T., 1999. *The Brain and Emotion*. Oxford University Press, Oxford.
- Rosen, W.G., Terry, R.D., Fuld, P.A., Katzman, R., Peck, A., 1980. Pathological verification of ischemic score in differentiation of dementias. *Ann. Neurol.* 7, 486–488. <https://doi.org/10.1002/ana.410070516>.
- Sanchez-Bornot, J.M., Wong-Lin, K.F., Ahmad, A.L., Prasad, G., 2018. Robust EEG/MEG based functional connectivity with the envelope of the imaginary coherence: sensor space analysis. *Brain Topogr.* 0, 1–22. <https://doi.org/10.1007/s10548-018-0640-0>.
- Schoffelen, J.-M., Gross, J., 2009. Source connectivity analysis with MEG and EEG. *Hum. Brain Mapp.* 30, 1857–1865. <https://doi.org/10.1002/hbm.20745>.
- Serrano-Pozo, A., Froehner, M.P., Masliah, E., Hyman, B.T., 2011. Neuropathological alterations in Alzheimer disease. *Cold Spring Harb. Perspect. Med.* 1. <https://doi.org/10.1101/cshperspect.a006189>.
- Smith, S.M., Nichols, T.E., 2009. Threshold-free cluster enhancement: addressing problems of smoothing, threshold dependence and localisation in cluster inference. *Neuroimage* 44, 83–98. <https://doi.org/10.1016/j.neuroimage.2008.03.061>.
- Styr, B., Slutsky, I., 2018. Imbalance between firing homeostasis and synaptic plasticity drives early-phase Alzheimer's disease. *Nat. Neurosci.* 21, 463–473. <https://doi.org/10.1038/s41593-018-0080-x>.
- Tewarie, P., Luzzi, L., O'Neill, G.C., Quinn, A.J., Griffa, A., Woolrich, M.W., Stam, C.J., Hillebrand, A., Brookes, M.J., 2019. Tracking dynamic brain networks using high temporal resolution MEG measures of functional connectivity. *Neuroimage* 200, 38–50. <https://doi.org/10.1016/j.neuroimage.2019.06.006>.
- Thompson, D.E., Mowla, M.R., Dhuyvetter, K.J., Tillman, J.W., Huggins, J.E., 2019. Automated artifact rejection algorithms harm P3 Speller brain-computer interface

- performance. *Brain Comput. Interfaces* 6, 141–148. <https://doi.org/10.1080/2326263X.2020.1734401>.
- van den Heuvel, M.P., Hulshoff Pol, H.E., 2010. Exploring the brain network: a review on resting-state fMRI functional connectivity. *Eur. Neuropsychopharmacol.* 20, 519–534. <https://doi.org/10.1016/j.euroneuro.2010.03.008>.
- Wang, H., Xie, K., Xie, L., Li, X., Li, M., Lyu, C., Chen, H., Chen, Y., Liu, X., Tsien, J., Liu, T., 2019. Functional brain connectivity revealed by sparse coding of large-scale local field potential dynamics. *Brain Topogr.* 32, 255–270. <https://doi.org/10.1007/s10548-018-0682-3>.
- Wechsler, D., 1997. *Wechsler Memory scale-III Manual*. Psychol. Corp., San Antonio, TX.
- Welsh, K., Butters, N., Hughes, J., Mohs, R., Heyman, A., 1991. Detection of abnormal memory decline in mild cases of Alzheimer's disease using CERAD neuropsychological measures. *Arch. Neurol.* 48, 278–281.
- Winkler, I., Brandl, S., Horn, F., Waldburger, E., Allefeld, C., Tangermann, M., 2014. Robust artifactual independent component classification for BCI practitioners. *J. Neural Eng.* 11 <https://doi.org/10.1088/1741-2560/11/3/035013>.
- Yu, M., Engels, M.M.A., Hillebrand, A., Van Straaten, E.C.W., Gouw, A.A., Teunissen, C., Van Der Flier, W.M., Scheltens, P., Stam, C.J., 2017. Selective impairment of hippocampus and posterior hub areas in Alzheimer's disease: an MEG-based multiplex network study. *Brain* 140, 1466–1485. <https://doi.org/10.1093/brain/awx050>.
- Zalesky, A., Fornito, A., Bullmore, E.T., 2010. Network-based statistic: identifying differences in brain networks. *Neuroimage* 53, 1197–1207. <https://doi.org/10.1016/j.neuroimage.2010.06.041>.
- Zalesky, A., Cocchi, L., Fornito, A., Murray, M.M., Bullmore, E., 2012a. Connectivity differences in brain networks. *Neuroimage* 60, 1055–1062. <https://doi.org/10.1016/j.neuroimage.2012.01.068>.
- Zalesky, A., Fornito, A., Egan, G.F., Pantelis, C., Bullmore, E.T., 2012b. The relationship between regional and inter-regional functional connectivity deficits in schizophrenia. *Hum. Brain Mapp.* 33, 2535–2549. <https://doi.org/10.1002/hbm.21379>.
- Zhang, F., Wu, W., Ning, L., McAnulty, G., Waber, D., Gagoski, B., Sarill, K., Hamoda, H. M., Song, Y., Cai, W., Rath, Y., O'Donnell, L.J., 2018. Suprathreshold fiber cluster statistics: leveraging white matter geometry to enhance tractography statistical analysis. *Neuroimage* 171, 341–354. <https://doi.org/10.1016/j.neuroimage.2018.01.006>.
- Zou, X., Coyle, D., Wong-Lin, K.F., Maguire, L., 2012. Beta-amyloid induced changes in A-type K⁺ current can alter hippocampo-septal network dynamics. *J. Comput. Neurosci.* 32, 465–477. <https://doi.org/10.1007/s10827-011-0363-7>.
- Zygmund, A., 2002. *Trigonometric Series*. Cambridge University Press.